Surface Engineering of EB-PBF Ti6Al4V via Anodization: Multifunctional Improvements Through TiO2 Nanotube Arrays

coatings

MDPI

*Article*

# Surface Engineering of EB-PBF Ti6Al4V via Anodization: Multifunctional Improvements Through $TiO_2$ Nanotube Arrays

**Alireza Moradi [1], Sanae Tajalli [2], Amir Behjat [3,4], Abdollah Saboori [3,4,*] and Luca Iuliano [3,4]**

[1] Department of Mechanical and Aerospace Engineering, Politecnico di Torino, Corso Duca Degli Abruzzi 24, 10129 Torino, Italy; s314119@studenti.polito.it
[2] Department of Applied Science and Technology, Politecnico di Torino, Corso Duca Degli Abruzzi 24, 10129 Torino, Italy; s314115@studenti.polito.it
[3] Department of Management and Production Engineering, Politecnico di Torino, Corso Duca degli Abruzzi 24, 10129 Torino, Italy; amir.behjat@polito.it (A.B.); luca.iuliano@polito.it (L.I.)
[4] Integrated Additive Manufacturing Center (IAM@PoliTo), Politecnico di Torino, Corso Castelfidardo 51, 10129 Torino, Italy
* Correspondence: abdollah.saboori@polito.it; Tel.: +39-0110907285

## Abstract

This study investigates the anodization behavior and surface modification of Ti6Al4V (Ti64) alloy components fabricated via electron beam powder bed fusion (EB-PBF), aiming to enhance their performance in biomedical applications. Ti64 samples were manufactured using optimized EB-PBF parameters to produce a uniform microstructure and surface quality. Electrochemical anodization at 40 V and 60 V for 2 h generated self-organized $TiO_2$ nanotube layers, followed by a heat treatment at 550 °C to improve crystallinity while preserving the nanotube morphology. Characterization using scanning electron microscopy (SEM) and atomic force microscopy (AFM) revealed that a lower voltage produced uniform, compact nanotubes with moderate roughness and higher hardness, whereas a higher voltage generated thicker, less ordered nanotubes with larger diameters, increased roughness, and slightly reduced mechanical performance. X-ray diffraction (XRD) confirmed the presence of anatase $TiO_2$ phases, and energy-dispersive spectroscopy (EDS) analysis revealed a homogeneous distribution of Ti and O. Mechanical testing via nanoindentation and nanoscratch techniques demonstrated superior hardness and adhesion in nanotubes formed at lower voltage due to their compact structure. Electrochemical measurements indicated significantly enhanced corrosion resistance in anodized samples, attributed to the dense and chemically stable $TiO_2$ layer that acts as a barrier to aggressive ions and reduces active corrosion sites. In vitro bioactivity analysis further confirmed improved apatite formation on anodized surfaces. These results demonstrate the synergistic potential of EB-PBF and controlled anodization for modifying the surface properties of Ti64 implants, leading to improved mechanical behavior, corrosion resistance, and biological performance suitable for biomedical applications.

**Keywords:** Ti6Al4V; electron beam powder bed fusion; anodization; nanotubes; biomedical applications; mechanical properties; corrosion behavior



Academic Editor: Przemysław Podulka

Received: 31 July 2025
Revised: 19 August 2025
Accepted: 21 August 2025
Published: 27 August 2025

**Citation:** Moradi, A.; Tajalli, S.; Behjat, A.; Saboori, A.; Iuliano, L. Surface Engineering of EB-PBF Ti6Al4V via Anodization: Multifunctional Improvements Through $TiO_2$ Nanotube Arrays. *Coatings* **2025**, *15*, 993. https://doi.org/10.3390/coatings15090993



## 1. Introduction

Ti6Al4V (Ti64) is one of the most widely used alloys in industrial applications due to its superior mechanical properties, high corrosion resistance, and good processability even at elevated temperatures [1,2]. Ti64 offers a high strength-to-weight ratio, making it suitable

for load-bearing implants such as femoral stems [3] and dental implants [4]. Furthermore, its passive oxide layer ($TiO_2$) protects the surface from aggressive ionic species in body fluids, providing long-term corrosion resistance and implant longevity [5,6]. However, despite these advantages, a major limitation of Ti64 in biomedical applications is its low bioactivity. Although the alloy is biocompatible and does not cause harmful or immunological reactions, it cannot form strong chemical bonds with surrounding tissue, which may potentially delay or impair osseointegration [7]. Therefore, surface functionalization is necessary to integrate the mechanical performance and biological interaction [8]. Among surface modification techniques, anodization has been recognized as a cost-effective and controllable method for modifying the surface oxide layer and forming $TiO_2$ nanotube arrays. This electrochemical treatment changes the surface morphology and chemistry by forming a thick and porous $TiO_2$ layer, which can be modified in terms of pore size, roughness, and topography [9]. These features are known to enhance hardness [10] and corrosion resistance [11,12]. Anodized surfaces can also serve as platforms for incorporating bioactive ions or molecules, offering additional functionalization for improved bone–implant integration [5]. While other methods are used, such as chemical etching [13], plasma spraying [14], and biomimetic coatings [15], Anodization is distinguished by its simplicity, reproducibility, and capacity for precise modification of surface characteristics required for biological performance [16–20].

Electron beam powder bed fusion (EB-PBF), an advanced technology, has significantly enhanced the production of biomedical implants by facilitating the creation of complex geometries that are challenging to produce with traditional methods [21–23]. This layer-by-layer process enables accurate control over porosity, microstructure, and density, which are key parameters for optimizing mechanical compatibility with the body and promoting tissue ingrowth. This flexibility for individualization is particularly advantageous in orthopedic and dental applications, where load-bearing capacity and biological integration are critical [24,25]. EB-PBF was selected instead of L-PBF for fabricating Ti64 implants due to several advantages, particularly relevant to biomedical applications. First, the high-vacuum environment reduces oxidation and contamination during melting, which is critical for achieving clean surfaces before anodization [26]. Second, the elevated powder bed preheating inherent to EB-PBF lowers cooling rates, thus reducing residual stresses and part distortion [27]. Then, higher beam power and multi-beam scanning enable faster build rates, making it efficient for fabricating complex components [28]. Among the materials processed with EB-PBF, Ti64 is known as the preferred material because of its excellent mechanical properties, corrosion resistance, and biocompatibility [24–26]. However, the EB-PBF process affects the microstructure of the fabricated components, depending on the process parameters and cooling rates [29–32]. Ti64 parts manufactured by EB-PBF typically develop either a fine $\alpha$-phase lamellar structure or acicular $\alpha'$ martensite, which differ considerably from the equiaxed microstructure found in wrought Ti64. These microstructural variations can have significant effects on both mechanical behavior and surface chemistry [29,33–35]. Furthermore, the as-built surfaces of EB-PBF components usually show high surface roughness and specific oxide layer properties due to the vacuum and high-temperature conditions within the EB-PBF chamber. These surface features are known to influence post-processing treatments, such as anodization, which are based on electrochemical reactions sensitive to surface composition, oxide thickness, and roughness [36]. As a result, the anodizing behavior and quality of $TiO_2$ nanotube arrays may differ significantly from those formed on conventionally manufactured Ti64 [17,37–40].

Although most anodizing research has focused on conventionally manufactured [17,39] or laser powder bed fusion (L-PBF) Ti64 substrates [9,18,41], the behavior of surfaces manufactured by EB-PBF under anodization conditions remains unexplored [11]. EB-

PBF provides distinct advantages compared to L-PBF in producing Ti64 substrates. The higher build temperatures and slower cooling rates of EB-PBF reduce residual stresses and minimize microstructural defects, resulting in more homogeneous, dense parts with improved fatigue performance [42]. Additionally, EB-PBF typically produces surfaces with partially melted particles and a unique distribution of oxide phases, which can influence subsequent surface modifications and mechanical behavior [43]. Recent studies have shown that EB-PBF surfaces, which typically feature partially melted particles and increased oxide phases, affect both the morphology and ordering of $TiO_2$ nanotube structures. For instance, Vásquez et al. [40] analyzed the impact of different manufacturing methods and anodizing conditions on the formation of $TiO_2$ nanotube layers on Ti64 alloy. They anodized samples at voltages of 15 V and 30 V to grow nanotube coatings and carefully analyzed the structure and corrosion resistance of the coating. Their findings showed that the cross-oriented EB-PBF surfaces had higher catalytic activity, enabling the growth of thicker and more uniform nanotube films compared to both the longitudinal EB-PBF and forged surfaces. On the other hand, Łępicka et al. [44] investigated how anodizing influences the corrosion resistance of Ti64 alloy, with a particular focus on the role of oxide-layer thickness in determining performance. They used untreated alloy samples and subjected them to anodizing at different voltages to generate oxide coatings of varying thickness and properties. They performed electrochemical polarization tests to measure corrosion rates and open-circuit potential measurements for stability assessment over time in a simulated saline environment. Their findings showed that anodizing generally improved the corrosion resistance of the alloy. However, unexpectedly, higher anodizing voltages and thicker oxide layers resulted in worse corrosion protection.

As for the surface modification for Ti64 substrates, various inorganic coatings have been extensively studied, including hydroxyapatite (HA) and bioglass [45–47]. These coatings aim to enhance bioactivity and osseointegration [48]. However, $TiO_2$ nanotube arrays, fabricated through anodization, offer unique advantages, especially when applied on Ti64 substrates produced via advanced AM techniques such as EB-PBF [49]. Additionally, the anodization process is cost-effective and allows for precise control over the nanotube dimensions, offering reproducibility and scalability [50]. Thus, our study focuses on the anodization of Ti64 substrates to form $TiO_2$ nanotubes, providing a cost-effective, reproducible, and bioactive surface modification that enhances the performance and longevity of titanium-based implants.

All in all, in this study, we addressed the limited research on Ti64 substrates fabricated using EB-PBF technology which offers distinct microstructural and surface features compared with conventional and L-PBF methods by thoroughly investigating their anodization response through comprehensive characterization, emphasizing how the EB-PBF-specific surface state influences the formation, morphology, and ordering of $TiO_2$ nanotube layers. This research demonstrates how anodization interacts with the surface, leading to the formation of nanostructured oxide layers that enhance implant functionality. Furthermore, our anodization process utilized an environmentally friendly aqueous electrolyte, highlighting a sustainable approach to implant surface functionalization. These findings provide valuable insights into the interplay between AM and post-processing, contributing to the development of advanced Ti-based implants.

## 2. Materials and Methods

### *2.1. Substrate Preparation*

Ti64 substrates were fabricated via EB-PBF using an ARCAM A2 system (Mölndal, Västra Götaland, Sweden). The fabrication process followed the standard Arcam A2X process parameters for Ti64, utilizing an accelerating voltage of 60 kV and a layer thickness

of 50 µm. During the EB-PBF process, a focus offset of 25 mA and a line offset of 200 µm were used. The feedstock material used for fabrication was spherical Ti64 powder. Figure 1a shows the powder morphology, and the size distribution is presented quantitatively in the histogram in Figure 1b. Scanning electron microscopy (SEM, Philips XL, Amsterdam, The Netherlands) analysis of the powder revealed uniformly spherical particles with smooth surfaces and a few attached satellites, while no internal porosity was observed. As illustrated in Figure 1b, the average particle size was 68 µm, with $d_{10}$ = 38 µm, $d_{50}$ = 55 µm, and $d_{90}$ = 88 µm.

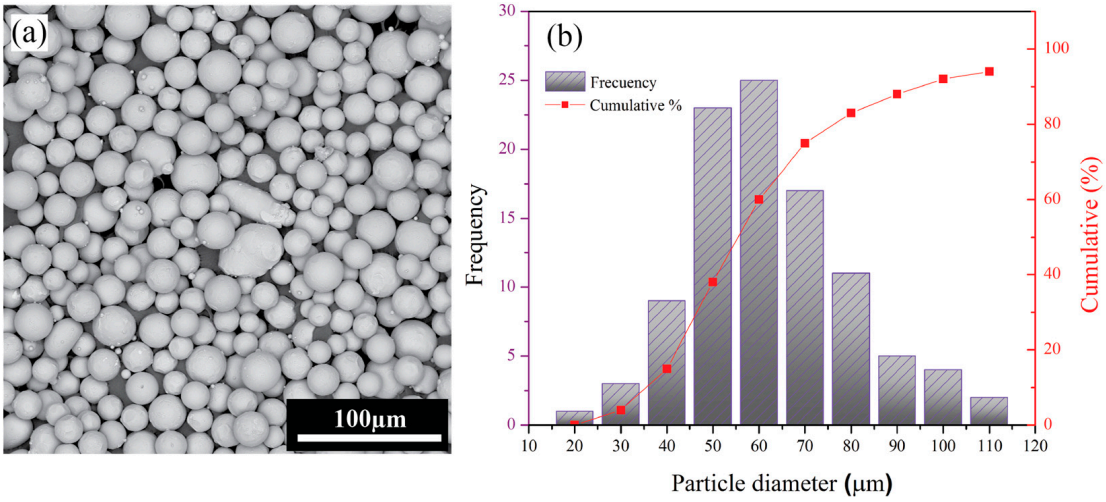


**Figure 1.** (**a**) SEM image of plasma-atomized Ti64 powder with spherical morphology; (**b**) particle-size distribution histogram.

### 2.2. Anodization

In this study, anodization was conducted at applied voltages of 40 V and 60 V. The anodization process was performed in a two-electrode configuration, with the EB-PBF Ti64 used as the anode (positive electrode) and stainless steel as the cathode (negative electrode). The electrolyte consisted of 90 vol.% ethylene glycol, 9 vol.% deionized water, and 82.8 mg of $NH_4F$ in a total volume of 30 mL. During anodization, the electrolyte bath temperature was maintained at 15–20 °C. Voltage was monitored by connecting a multimeter in parallel with the circuit, while an ammeter in series measured the current during the process. The electrodes were spaced 3 cm apart in the anodization bath, and the process was conducted for 2 h. Upon completion, the anodized samples were immersed in a bath containing a mixture of deionized water and ethanol for 10 min in the ultrasonic cleaner. Finally, the specimens were dried in a furnace at 550 °C for 2 h. Figure 2 shows a schematic representation of the process.

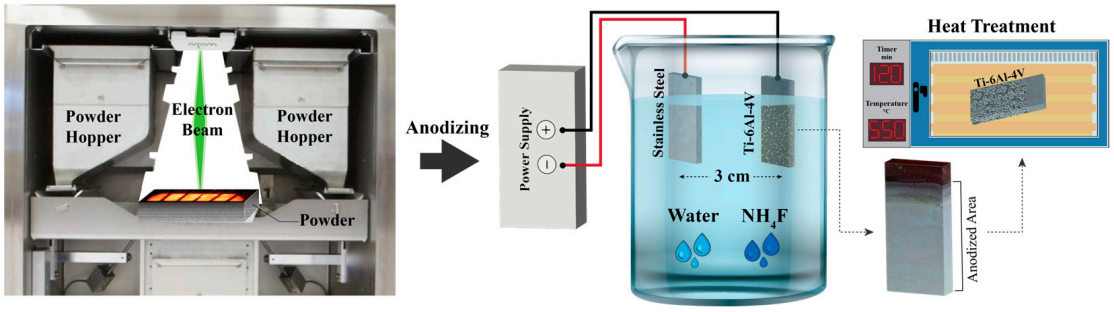


**Figure 2.** Process flow for fabricating and anodizing EB-PBF Ti64 samples.

### *2.3. Characterization Methods*

#### 2.3.1. Surface Characterization

The microstructure and surface characteristics of the as-built Ti64 substrates produced by EB-PBF, as well as the $TiO_2$ nanotube coatings formed by anodization at 40 V and 60 V, were investigated through multiple complementary techniques. Optical microscopy (OM) and SEM were employed to examine the substrate microstructure before coating and to assess the nanotube arrays after anodization. The elemental composition and distribution on the anodized surfaces were analyzed by energy dispersive spectroscopy (EDS) using an Oxford Instruments detector at 20 kV. Structural analysis of the as-built Ti64 and oxide layers was conducted using X-ray diffraction (XRD, Phillips, Amsterdam, Netherlands), employing Cu Kα radiation (λ = 1.54 nm) and scanning from 2θ = 10° to 90°.

#### 2.3.2. Atomic Force Microscopy (AFM) Test

For evaluation of the surface analysis, topographical texture, and scars of Ti64 samples, atomic force microscopy (AFM) was conducted using a Nanoscope III (ARA research, BRISK 2019, Tehran, Iran) in areas of 5 × 5 μm.

#### 2.3.3. Nanoindentation Test

Nanoindentation experiments were conducted to evaluate the hardness and elastic modulus of the $TiO_2$ using a nanomechanical test instrument (Hysitron Inc., TriboScope®, Minneapolis, MN, USA) with a 2D transducer. The tests were conducted using a Berkovich diamond indenter in Continuous Stiffness Measurement (CSM) mode. This testing configuration provides the continuous measurement of elastic contact stiffness (S) during loading, generating depth profiles for both modulus and hardness.

#### 2.3.4. Nanoscratch Test

Nanoscratch testing was conducted to evaluate the adhesion strength and mechanical properties of $TiO_2$ nanotube coatings formed on Ti64 as-built samples anodized at 40 V and 60 V. Figure 3 shows a schematic illustration of the nanoscratch test setup and procedure. For each modified sample, three nanoscratch tests were performed on distinct surface regions to ensure reproducibility. The scratch length was set to 500 μm, and an increasing normal load was applied progressively. During the test, continuous measurements of the normal force, lateral force, and friction coefficient were recorded to detect the onset of coating failure.

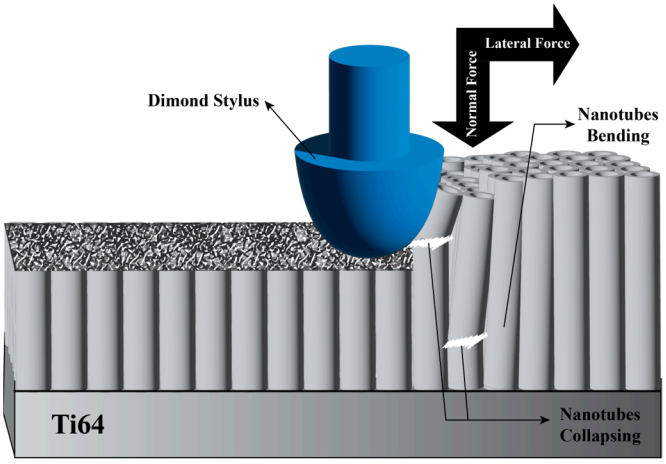


**Figure 3.** Schematic illustration of the nanoscratch test performed on the modified surface.

2.3.5. Corrosion Test

The corrosion characteristics were investigated using a PARASTAT 2273 (Princeton Applied Research, TN, USA). Prior to electrochemical measurements, the specimens were immersed in simulated bodily fluid (SBF) prepared according to the composition proposed by Kokubo et al. [51] at a constant temperature of 37° with a pH of 7.2 for 30 min to stabilize the surface condition. A three-electrode electrochemical cell configuration was applied, using a saturated Ag/AgCl as the reference electrode, a platinum plate as the counter electrode, and the prepared sample as the working electrode. The open-circuit potential (OCP) was measured for 30 min. Then, electrochemical impedance spectroscopy (EIS) was performed on the OCP, applying a sinusoidal signal of 10 mV of amplitude with a frequency scan from 100 kHz to 10 mHz. The resulting EIS data were subsequently analyzed and fitted using Z-View v.40h software (AMETEK, Inc, Berwyn, IL, USA). Finally, potentiodynamic polarization (PDP) testing was performed by sweeping the potential, commencing at −0.25 mV relative to a saturated Ag/AgCl reference electrode, with a scanning rate of 1 mV/s.

2.3.6. In Vitro Bioactivity

The in vitro bioactivity of the $TiO_2$ nanotube structures was evaluated by analyzing their ability to induce HA formation on the sample surfaces. The samples were immersed in SBF to mimic physiological conditions. The specimens were maintained at 37 °C for 14 days with a surface area-to-volume ratio of 1 $cm^2$/mL. Following the retrieval of the samples from the SBF, they were rinsed with distilled water and subsequently dried in an oven. To assess the surface morphology and composition of the samples, SEM and EDS were employed to confirm the formation of HA.

## 3. Results and Discussion

### *3.1. Microstructure of EB-PBF Ti64 Alloy*

The characterization of Ti64 after EB-PBF, illustrated in Figure 4, was performed using XRD, OM, and SEM. XRD patterns mainly showed peaks corresponding to the α/α′-phase, with smaller peaks indicating retained β-phase, demonstrating the biphasic nature typical for Ti64 processed by EB-PBF, as confirmed by SEM. Microstructure analysis provided a detailed understanding of the characteristics of Ti64 parts produced by EB-PBF. Typical features were observed, including melt pool boundaries formed during layer-by-layer solidification, columnar prior-β grains oriented along the build direction, and fine α-phase structures resulting from rapid cooling [24].

The EDS analysis, shown in Figure 5, was conducted on the highlighted region to verify the elemental composition. The detected elements include titanium (Ti), aluminum (Al), and vanadium (V), consistent with the nominal composition of Ti64. This confirms the integrity and compositional uniformity of the alloy after the EB-PBF process. Minor deviations from the nominal values may be attributed to localized microstructural variations or measurement limitations associated with the EDS technique.

### *3.2. Surface Morphology After Modifications*

Figure 6 shows the XRD pattern of the specimen anodized for 120 min. After anodization, additional peaks related to crystalline $TiO_2$ appeared, verifying the successful formation of nanotubes [52]. Prior studies have demonstrated that anodization can yield substoichiometric titanium oxide phases such as $TiO_2$ on the surface [53]. It is worth mentioning that besides $TiO_2$, the anodized oxide layer typically exists in an amorphous form immediately after fabrication. The subsequent heat treatment used in this study facilitates crystallization into defined $TiO_2$ polymorphs [54,55]. The anatase structure is of particular

interest for biomedical applications, as it has been shown to enhance surface energy, protein adsorption, and bioactivity compared to rutile. Therefore, controlling the post-anodization heat treatment is critical for modifying the crystallographic composition of the nanotube layer to optimize biological performance [56].

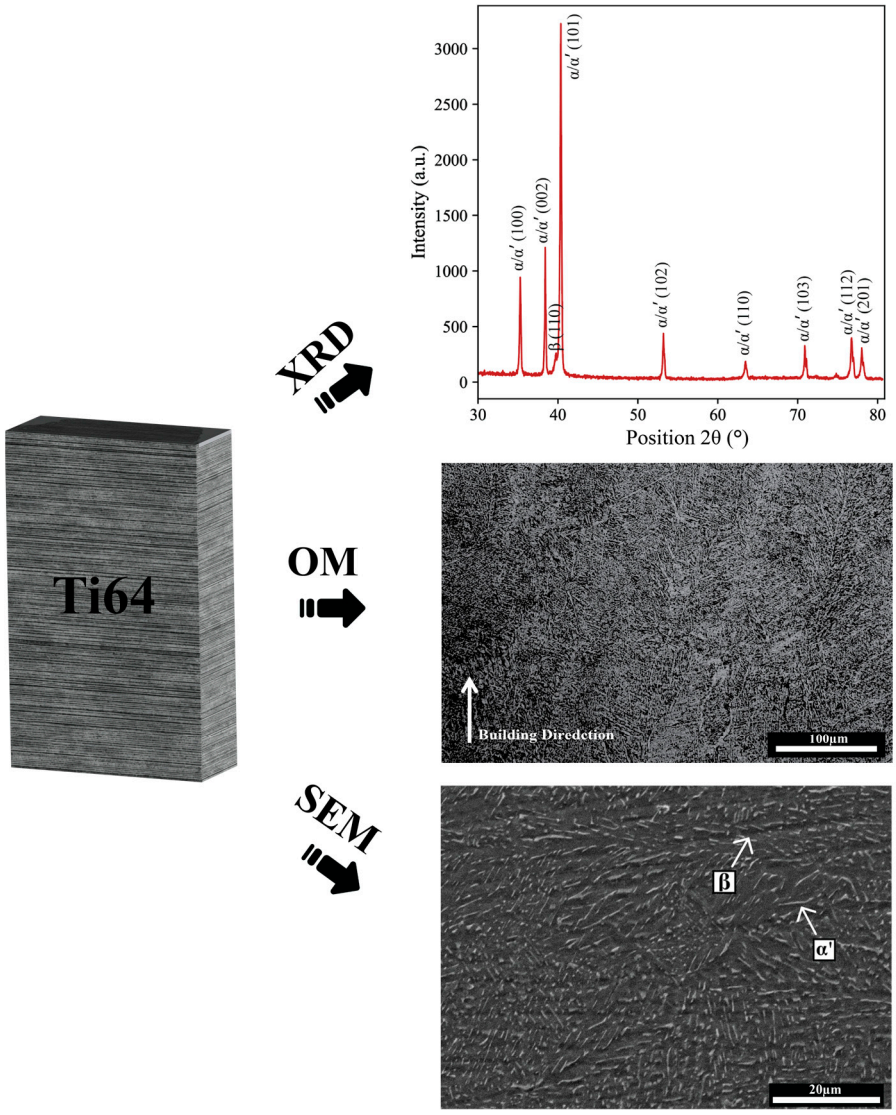


**Figure 4.** Microstructure and phase analysis of EB-PBF Ti64 using OM, SEM, and XRD before anodization.

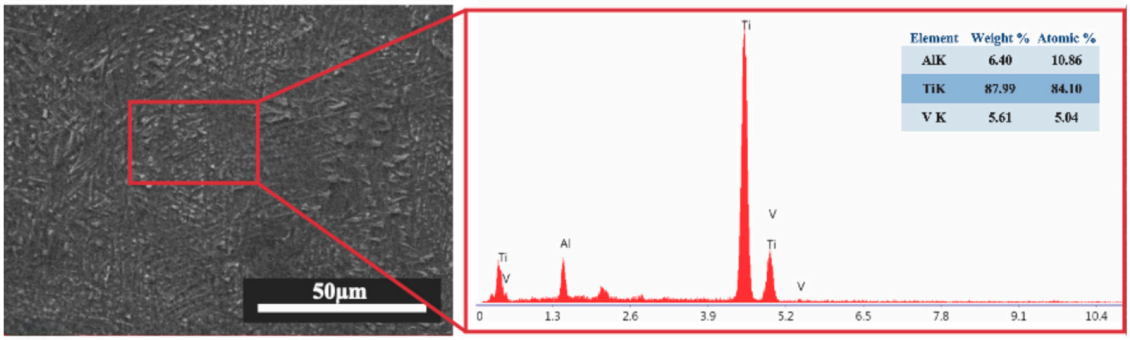


**Figure 5.** SEM micrograph and corresponding EDS spectrum of EB-PBF Ti64.

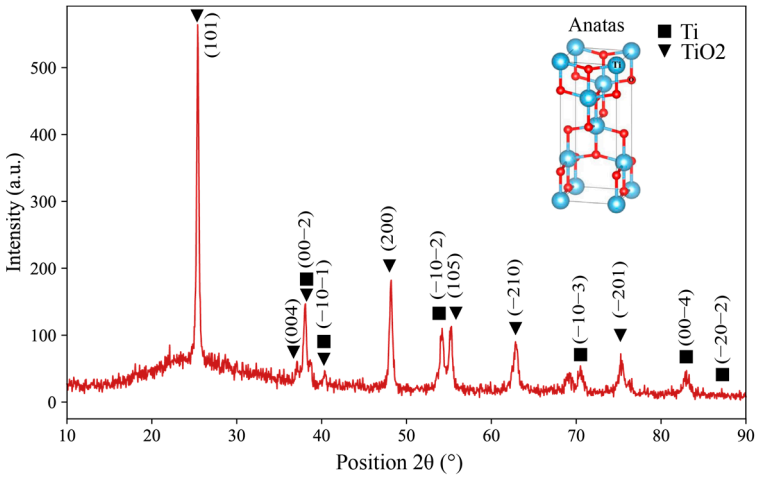


**Figure 6.** XRD pattern of $TiO_2$ formed on the EBPBF Ti64 alloy.

SEM images of Ti64 surfaces anodized at 40 V (Figure 7a,b) and 60 V (Figure 7c,d) reveal the morphological evolution of $TiO_2$ nanotube arrays with increasing anodization voltage. At 40 V, the nanotubes exhibit a relatively uniform, well-organized, and densely packed array with consistent diameters, indicating favorable self-organization during the anodization process. In contrast, the samples anodized at 60 V show nanotube arrays with larger diameters and less uniform distribution. The tubes appear more irregular and loosely packed, with increased structural disorder, which may be attributed to more aggressive oxide growth and dissolution dynamics at higher voltages. Therefore, it can be concluded that the increase in anodization voltage from 40 V to 60 V led to the growth of larger nanotube diameters and thicker oxide layers based on nanotube diameter and depth, consistent with the enhanced oxidation kinetics at higher potentials. The morphological changes suggest that while higher voltages promote tube growth, they may also disrupt the balance between oxide formation and dissolution, potentially compromising the uniformity of the nanotube structure [57]. The schematic in Figure 7e illustrates the anodization mechanism for the formation of $TiO_2$ nanotube arrays. In detail, when a voltage is applied, the titanium surface undergoes oxidation, forming a compact oxide layer. Simultaneously, fluoride ions ($F^-$) in the electrolyte chemically dissolve the oxide layer [58]. This balance between oxide growth and localized dissolution leads to pore formation, followed by self-organization into nanotubular structures.

Nanotube dimensions, including diameter and depth, are detailed in Table 1, which are also shown in Figure 8a,b.

**Table 1.** Average thickness and average diameter of $TiO_2$ nanotube array layers produced at different voltages.

| Potential (V) | Nanotube Diameter (nm) | Nanotube Depth (nm) |
|---|---|---|
| 40 | 72.95 | 145.26 |
| 60 | 80.47 | 442.03 |

EDS analysis was used to analyze the chemical composition of the anodized surface. The presence of titanium (Ti) and oxygen (O) was confirmed, which is primarily associated with the $TiO_2$ nanotubes, as shown in Figure 8c. These elements were uniformly distributed across the nanotube surfaces for both 40 V and 60 V anodization conditions, indicating compositional homogeneity. Trace elements present in the raw data were not included in the figure for clarity, as their contributions are negligible.

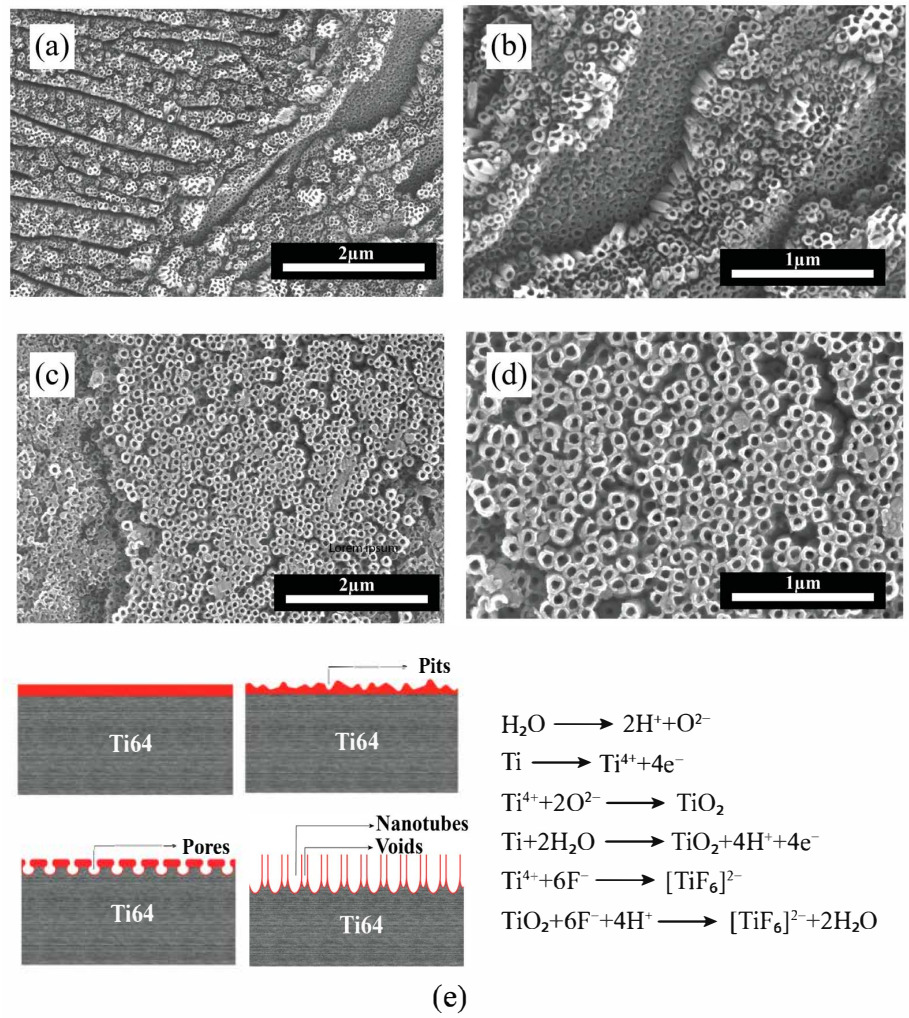


**Figure 7.** SEM images of $TiO_2$ nanotube formation on EB-PBF Ti64 alloy. (**a**,**b**) at 40 V and (**c**,**d**) at 60 V; (**e**) schematic illustration of anodization mechanism and reactions.

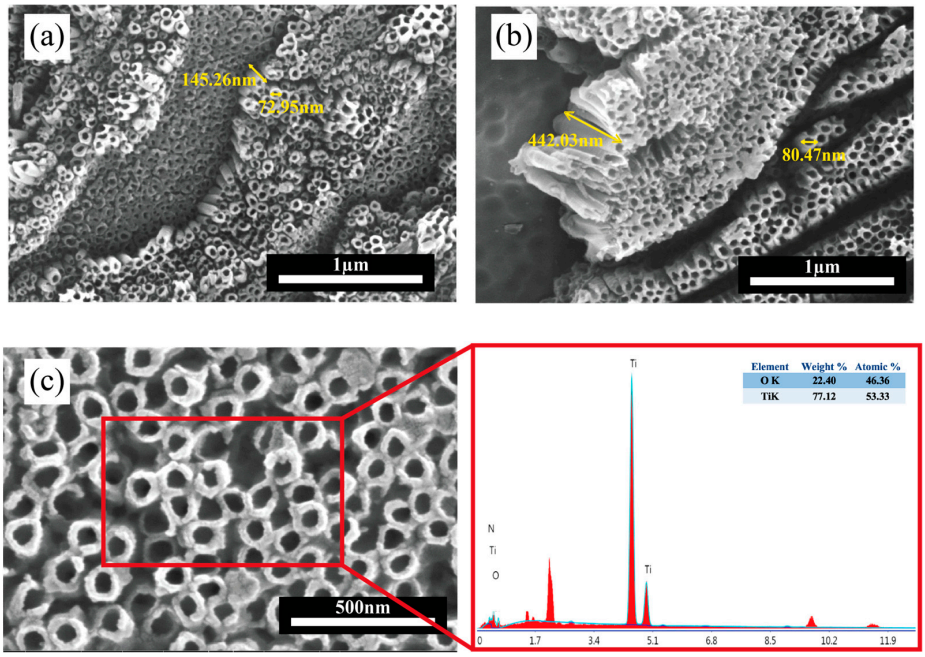


**Figure 8.** SEM images of $TiO_2$ nanotube arrays formed on Ti64 at (**a**) 40 V; (**b**) 60 V anodization voltages; (**c**) high-resolution SEM image with corresponding EDS elemental analysis.

### *3.3. AFM Analysis of the Surfaces*

AFM images analyze the roughness and topographical properties of the nanotube surfaces created on Ti64 anodized at two different voltages. Figure 9 illustrates both 2D and 3D AFM images of the surface topographies of the Ti64 anodized sample. As can be seen in Figure 9a,b, the sample anodized at 40 V exhibits a relatively uniform nanotube surface with moderate roughness, while the 60 V anodized surface (Figure 9c,d) demonstrates a more irregular topography with higher surface asperities and deeper valleys and higher peaks in the 0–300 nm range, indicating a wider surface height distribution. This difference is reflected in the root mean square (RMS) roughness values, which increased from 95 nm at 40 V to 127 nm at 60 V, indicating a significant increase in nanoscale surface texture with voltage.

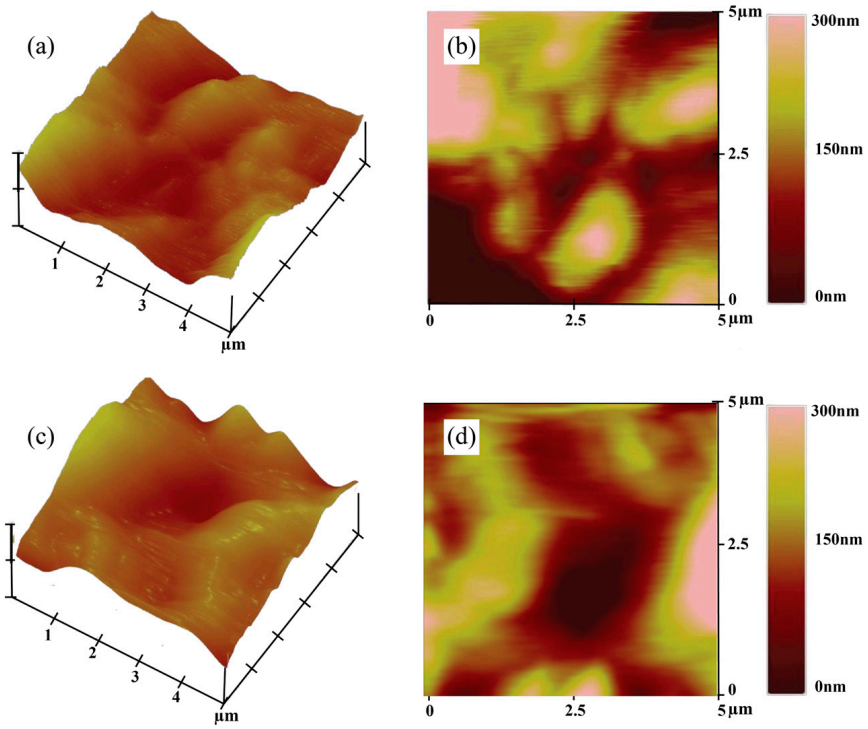


**Figure 9.** Topographic AFM images of the Ti64 samples: (**a**,**c**) 3D topography and (**b**,**d**) 2D height map of the surface anodized at 40 V and 60 V, respectively.

### *3.4. Nanoindentation Tests of the Surface*

Nanoindentation analysis demonstrated the distinct mechanical characteristics of the $TiO_2$ nanotube-coated specimens anodized at 40 V and 60 V. Figure 10 displays the load–displacement curves, which provides real-time acquisition of hardness and modulus as a function of penetration depth. As illustrated, both anodized samples showed continuous loading and unloading curves characterized by smooth profiles without abrupt discontinuities, indicating stable indentation behavior and the absence of surface fracture or delamination during testing.

The 40 V anodized sample demonstrated a higher resistance to indentation, reaching a maximum load at a lower penetration depth (~350 nm), in contrast to the 60 V sample, which required deeper penetration (~440 nm) under similar loading conditions. This suggests a stiffer and harder oxide layer in the 40 V sample, consistent with the calculated hardness and modulus values, 0.21 GPa and 32 GPa, respectively, compared to 0.16 GPa and 30 GPa for the 60 V sample (Table 2). These differences are also evident in the steeper unloading slope observed in the 40 V curve, which supports its higher elastic modulus. The reduction in hardness and stiffness observed for the 60 V sample may be caused by

its increased surface roughness and morphological irregularity, as previously discussed in Section 3.3. Higher surface roughness may lead to localized stress concentrations and diminished load-bearing capacity, reducing the mechanical integrity of the nanotube layer. Additionally, the larger contact area and lower density of the nanotube walls at higher anodization voltages may contribute to this mechanical softening.

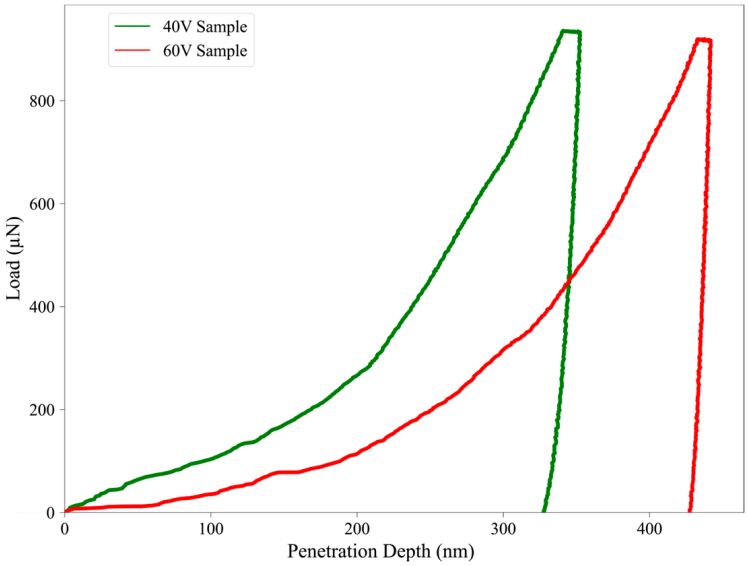


**Figure 10.** Load–penetration depth curves at 40 V (green) and 60 V (red).

**Table 2.** Surface and mechanical properties for Ti64 anodized samples.

| Potential (V) | H (GPa) | Er (GPa) | Friction Coefficient | RMS (nm) |
|---|---|---|---|---|
| 40 | 0.21 ± 0.04 | 32 ± 0.8 | 0.75 ± 0.12 | 95 ± 3 |
| 60 | 0.16 ± 0.06 | 30 ± 1.2 | 0.85 ± 0.18 | 127 ± 5 |

The indentation behavior also supports the presence of viscoelastic or plastic deformation, particularly in the 60 V sample, as indicated by the broader separation between loading and unloading curves. According to the literature, if the final penetration depth-to-peak-depth ratio ($h_f/h_{max}$) exceeds 0.7, pile-up effects may influence the hardness calculation. In this study, both samples showed $h_f/h_{max} < 0.7$, indicating sink-in behavior and confirming the validity of the extracted mechanical values without significant overestimation due to pile-up effects [59].

Overall, the nanoindentation results reinforce the correlation between anodization voltage, nanotube morphology, and mechanical performance. The denser and more uniform nanotube array at 40 V provides improved hardness and stiffness, whereas the rougher, more irregular surface at 60 V compromises the mechanical properties despite the thicker oxide layer.

### *3.5. Scratch Testing*

The adhesion and cohesion behavior of the $TiO_2$ nanotube coatings on Ti64 substrates was evaluated via progressive load nanoscratch testing. The critical loads (Lc), marking the onset of cohesive or adhesive failure, were measured at approximately 3.0 N for the 40 V coating and around 4.5 N for the 60 V coating. This suggests enhanced interfacial adhesion in the 60 V sample, likely due to increased film thickness and better mechanical interlocking with the substrate [60].

In terms of friction performance, the coating produced at 40 V showed an average friction coefficient of 0.75, while the 60 V coating had a slightly higher coefficient of 0.85. The increased friction for the 60 V sample can be attributed to its greater surface roughness (RMS = 127 nm vs. 95 nm), which increases the number of contact points during scratch testing. Compared to the uncoated Ti64 substrate, which showed early failure and marked pile-up deformation under the indenter, the anodized coatings exhibited substantially improved scratch resistance and mechanical integrity [61].

Table 2 summarizes the surface and mechanical properties obtained from the above analysis for the Ti64 samples anodized at 40 V and 60 V, highlighting the effect of anodization voltage on roughness and tribo-mechanical behavior. The results indicate a significant correlation between surface roughness and tribomechanical behavior. The higher roughness observed at 60 V results in increased surface interaction and contact area, which could explain the higher friction coefficient and the corresponding decrease in hardness. This behavior is aligned with the literature, where increased surface roughness is often correlated with higher friction and lower mechanical resistance. These effects are primarily due to the more distinct surface irregularities and localized stress concentrations during indentation or sliding [32].

### *3.6. Electrochemical Characterization*

The electrochemical behavior of the Ti64 samples, both in their as-built and anodized (40 V and 60 V) states, was assessed through PDP and EIS in SBF. The polarization curves in Figure 11a demonstrate a significant improvement in corrosion resistance for the anodized samples compared to the EB-PBF Ti64. The electrochemical parameters, specifically corrosion current density ($I_{corr}$), passive current density ($I_{pass}$), and corrosion potential ($E_{corr}$), obtained from the polarization curves are presented in Table 3. Both anodized samples show a more positive $E_{corr}$ and reduced $I_{corr}$, indicating enhanced passivation due to the formation of protective oxide layers. Notably, the sample anodized at 60 V exhibits the lowest $I_{corr}$. In EB-PBF Ti64, with the increase in the potential from $\approx$ 1.32 V, the current density suddenly increased, which is caused by the loss of the passive layer in this sample and the decrease in corrosion resistance. In contrast, the anodized samples exhibit comparable corrosion potentials. This observation indicates a heightened corrosion resistance in these particular anodized samples.

**Table 3.** Electrochemical parameters of the samples based on the PDP curve in the SBF solution.

| Samples | $I_{corr}$ (μA/cm$^2$) | $I_{pass}$ (μA/cm$^2$) | $E_{corr}$ (V) |
|---|---|---|---|
| Base sample | $0.81 \pm 0.04$ | - | $-0.42 \pm 0.07$ |
| 40 V sample | $0.12 \pm 0.02$ | $12.12 \pm 0.12$ | $-0.27 \pm 0.04$ |
| 60 V sample | $0.04 \pm 0.02$ | $11.23 \pm 0.23$ | $-0.15 \pm 0.08$ |

The electrochemical impedance spectra, represented by the Nyquist plot (Figure 11b) and Bode-phase plot (Figure 11c), further demonstrate the superior performance of the anodized samples. As illustrated in Figure 11b, anodized samples exhibit inadequate capacitive semicircles, indicating their effectiveness as barriers against the diffusion of corrosive solutions. The largest diameter of the capacitive semicircles is associated with the sample subjected to a 60 V. Following this, the samples with 40 V rank next in terms of semicircle diameter. Conversely, the base sample demonstrates the smallest semicircle diameter, reflecting its inferior corrosion resistance. Indeed, the Nyquist plots for anodized samples show two distinct capacitive loops, suggesting the presence of two-time constants associated with the oxide film and the double-layer interface. The Bode-phase plot (Figure 11c) also reveals a broader and higher phase angle plateau for the 60 V sample,

indicating enhanced dielectric properties and a more capacitive behavior, consistent with a denser and more protective anodic oxide film. This improved impedance response confirms the formation of a homogeneous and adherent oxide coating on the anodized EB-PBF Ti64 samples [40]. Also, the Bode-phase diagram for the 60 V anodizing exhibits two distinct peaks: one located near 0.1 Hz and another extending into frequencies exceeding 100 Hz. The peak observed at lower frequencies is primarily attributed to the thin and dense oxide layer that forms on the surface of the oxidized substrate. In contrast, the peak at higher frequencies is associated with the porous structure of the titanium dioxide nanotubes. The comprehensive body of evidence indicates that the 60 V sample exhibits superior performance in terms of corrosion resistance and coating efficacy.

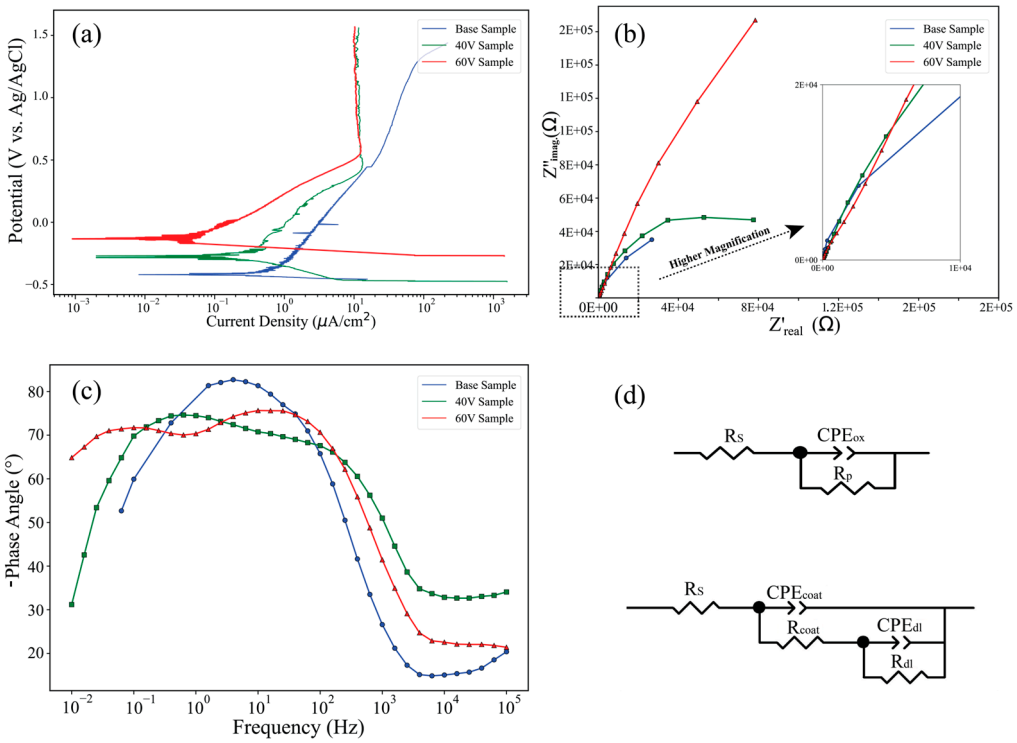


**Figure 11.** Electrochemical characterization of EB-PBF Ti64 and anodized samples: (**a**) PDP curves; (**b**) Nyquist plots with high-frequency inset; (**c**) Bode-phase angle plots; (**d**) equivalent circuit models for base and anodized samples.

Two equivalent circuits (Figure 11d) were proposed to describe the experimental data. As depicted, the electrochemical circuit (EC) model was characterized by a single time constant, specifically for the base Ti64 sample. In contrast, a two-time-constant model was employed to accurately fit the experimental impedance data acquired from anodized samples. The components depicted in Figure 11d are defined as follows: $R_s$ represents the uncompensated resistance of the test electrolyte situated between the working and reference electrodes. $R_p$ ($R_{coat}$) denotes the polarization resistance at the interface between the electrode and the electrolyte, as well as the resistance of the oxide layer for other samples. $R_{dl}$ indicates the pore resistance of the nanotubes. $CPE_{ox}$ ($CPE_{coat}$) refers to the capacitance associated with the oxide film, while $CPE_{dl}$ pertains to the capacitance of the nanotubes and the double-layer capacitance and charge-transfer resistance. Notably, a constant phase element (CPE) is employed in place of a pure capacitance due to the presence of inhomogeneities in the distribution of relaxation times at the microscopic level on the electrode surface. The impedance of the CPE is mathematically expressed as follows:

$$Z_{CPE} = Q(\omega^{n}j)^{-1} \quad (1)$$

where Q, j, and ω represent the magnitude of the CPE, the imaginary unit, and the angular frequency, respectively. Table 4 shows the electrochemical parameters obtained from EIS spectra using the equivalent circuits in Figure 11d. Considering the data in Table 4, higher values of $R_p$ ($R_{coat}$) than $R_{dl}$ indicated the high compactness and better passivity of the surface compared to porous nanotubes. The overall results demonstrate that anodization at 60 V leads to significantly improved corrosion resistance compared to the base and 40 V anodized conditions.

**Table 4.** Electrical element values were obtained by fitting the EIS plots.

| Sample | $R_s$ ($\Omega.cm^2$) | $CPE_{dl}$ ($\mu F/cm^2.sn^1$) | $CPE_{ox/coat}$ ($\mu F/cm^2.sn^1$) | $R_{dl}$ ($\Omega.cm^2$) | $R_{ox/coa}$ ($k\Omega.cm^2$) |
|---|---|---|---|---|---|
| Base sample | 10.8 | - | 56.12 ± 0.05 | - | 78.70 ± 0.08 |
| 40 V sample | 8.29 | 0.31 ± 0.03 | 76.48 ± 0.13 | 31.52 ± 0.05 | 303.71 ± 1.45 |
| 60 V sample | 11.98 | 1.24 ± 0.02 | 58.34 ± 0.11 | 42.49 ± 0.04 | 802.41 ± 2.23 |

### *3.7. In Vitro Apatite Formation*

The in vitro bioactivity of the $TiO_2$ nanotube surfaces is primarily related to their ability to facilitate HA formation when immersed in SBF. The process begins with the adsorption of calcium ions ($Ca^{2+}$) from the SBF onto the negatively charged surface of the nanotubes, followed by the integration of phosphate ions ($PO_4{}^{3-}$), resulting in the formation of a layer rich in calcium phosphate. Over the immersion period, typically 14 days, this amorphous phase gradually transforms into a crystalline HA layer through a solution-mediated precipitation reaction, represented by

$$10\ Ca^{2+} + 6PO_4{}^{3-} + 2OH^{-} \rightarrow Ca_{10}\ (PO_4)_6\ (OH) \quad (2)$$

The nanotubular morphology significantly enhances this process by offering a high surface area, improved ion exchange capacity, and favorable surface energy, all of which contribute to the accelerated nucleation and uniform growth of HA. This bioactive surface modification is considered as a critical indicator of the material's potential for osseointegration and bone-bonding performance in biomedical applications [62]. It is well recognized that forming a bone-like apatite layer on metallic surfaces immersed in body fluids is essential for indicating favorable biological interactions and achieving reliable bone bonding [63]. Figure 12 presents the surface morphology and elemental composition of anodized samples after immersion in SBF for 14 days. As shown in Figure 12a,b, the surface retains its porous nanotubular structure, with apatite deposition clearly visible, and there is no obvious difference between the two samples. A closer view reveals the formation of densely packed, globular apatite clusters distributed across the surface. Figure 12c provides a high-magnification image of the red-marked region from Figure 12b, confirming the presence of uniform, flower-like HA particles coating the nanotubes. The corresponding EDS spectrum in Figure 12d verifies the presence of calcium (Ca) and phosphorus (P) as dominant elements in the deposited layer. The calculated Ca/P atomic ratio is approximately 1.53, indicating the formation of a calcium-rich phosphate phase, which is consistent with HA. These results demonstrate that the nanotubular coating, combined with appropriate thermal treatment, provides a bioactive surface capable of supporting apatite formation, highlighting its potential application in bone-interfacing biomedical implants [64].

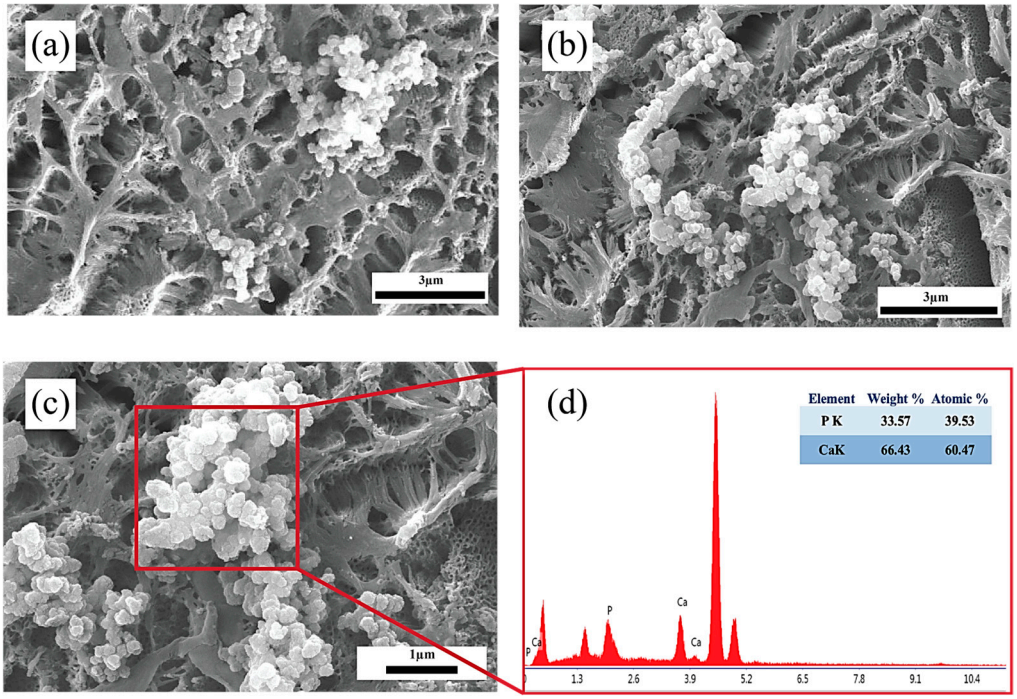


**Figure 12.** SEM images of $TiO_2$ nanotube-coated surfaces after 14 days of immersion in SBF: (**a**) 40 V; (**b**) 60 V; (**c**) high-magnification view of (**b**); and (**d**) EDS analysis confirming the existence of Ca and P elements.

## 4. Conclusions

This work successfully investigated the surface modification of EB-PBF Ti64 alloy using anodization to fabricate $TiO_2$ nanotube coatings. The findings led to the following conclusions:

- Structural characterization via SEM, XRD, and EDS confirmed the formation of nanotubes with distinct morphologies depending on the applied voltage and demonstrated the presence of crystalline $TiO_2$ phases.
- At 40 V, anodization resulted in uniform, well-organized nanotube arrays with moderate roughness and superior mechanical properties, including higher hardness and stiffness. In contrast, anodization at 60 V produced thicker, less ordered nanotubes with larger diameters, increased roughness, and slightly reduced mechanical performance, likely due to morphological irregularities and structural disorder.
- AFM and nanoindentation analyses confirmed that increasing anodization voltage increased surface roughness while decreasing hardness and modulus. Higher roughness at 60 V also led to increased friction coefficients, showing a clear correlation between topography and tribo-mechanical behavior.
- Electrochemical characterization showed both anodized samples outperformed the base material in corrosion resistance, with the 60 V sample showing the best performance due to its denser oxide layer and greater impedance, as confirmed by EIS and potentiodynamic polarization.
- In vitro bioactivity studies in SBF demonstrated that both anodized and heat-treated surfaces supported apatite formation after 14 days of immersion. SEM and EDS analyses confirmed the deposition of a calcium phosphate layer, validating the biological potential of the $TiO_2$ nanotube coatings.
- All in all, this study demonstrated anodization as an effective post-processing technique for enhancing the surface properties of Ti64 components.

**Author Contributions:** Conceptualization, A.S. and A.B.; methodology, A.B., S.T. and A.M.; validation, A.S., L.I. and A.B.; formal analysis, A.B.; data curation, A.B., S.T. and A.M.; writing—original draft preparation, A.B., S.T. and A.M.; writing—review and editing, A.S., L.I., and A.B.; visualization, A.S. and A.B.; supervision, A.S. and A.B.; funding acquisition, A.S. and L.I. All authors have read and agreed to the published version of the manuscript.

**Funding:** This research received no external funding.

**Institutional Review Board Statement:** Not applicable.

**Informed Consent Statement:** Not applicable.

**Data Availability Statement:** The original contributions presented in the study are included in the article, further inquiries can be directed to the corresponding author.

**Conflicts of Interest:** The authors declare no conflicts of interest.

## References

1. Onuike, B.; Bandyopadhyay, A. Additive manufacturing of Inconel 718—Ti6Al4V bimetallic structures. *Addit. Manuf.* **2018**, *22*, 844–851. [CrossRef]
2. Bandekhoda, M.R.; Mosallanejad, M.H.; Atapour, M.; Iuliano, L.; Saboori, A. Investigation on the Potential of Laser and Electron Beam Additively Manufactured Ti–6Al–4V Components for Orthopedic Applications. *Met. Mater. Int.* **2024**, *30*, 114–126. [CrossRef]
3. Mehboob, H.; Tarlochan, F.; Mehboob, A.; Chang, S.-H.; Ramesh, S.; Harun, W.S.W.; Kadirgama, K. A novel design, analysis and 3D printing of Ti-6Al-4V alloy bio-inspired porous femoral stem. *J. Mater. Sci. Mater. Med.* **2020**, *31*, 78. [CrossRef]
4. Akshay Kumar, J.; Jaya Prakash, K.; Shivraj Narayan, Y.; Satyanarayana, B. FE-strength evaluation of Ti-6Al-4V alloy dental implant and 3D printing using PLA material. *Mater. Today Proc.* **2023**, *in press*. [CrossRef]
5. Goli, M.; Shahrebabaki, K.E.; Mehrnoush, S.; Labbaf, S. Characterization of $TiO_2$ nanotube formation on additively manufactured Ti6Al4V surfaces for medical implants. *J. Mater. Res.* **2025**, *40*, 622–636. [CrossRef]
6. Behjat, A.; Sanaei, S.; Mosallanejad, M.H.; Atapour, M.; Saboori, A. Electrochemical Behavior of Electron Beam Powder Bed Fused Ti536 Alloy under Simulated Inflammatory Conditions. *Acta Metall. Sin. Engl. Lett.* **2025**, *38*, 969–980. [CrossRef]
7. Zhao, L.; Chu, P.; Zhang, Y.; Wu, Z. Antibacterial Coatings on Titanium Implants. *J. Biomed. Mater. Res. B Appl. Biomater.* **2009**, *91*, 470–480. [CrossRef] [PubMed]
8. de Sousa, T.K.C.; Maia, F.R.; Pina, S.; Reis, R.L.; Oliveira, J.M.; Carobolante, J.P.A.; Escada, A.L.D.A.; Longhitano, G.A.; Alves, A.P.R. Anodic Oxidation of 3D Printed Ti6Al4V Scaffold Surfaces: In Vitro Studies. *Appl. Sci.* **2024**, *14*, 1656. [CrossRef]
9. Crenn, M.J.; Lefort, L.; Pires, R.; Dubot, P.; Giorgi, M.L.; Peyre, P. Anodized SLM Ti6Al4V surface: Influence of surface characteristics on NTs growth and resulted surfaces properties. *J. Mater. Chem. B.* **2024**, *12*, 11502–11514. [CrossRef] [PubMed]
10. Zhang, L.; Chen, L.Y.; Wang, L. Surface Modification of Titanium and Titanium Alloys: Technologies, Developments, and Future Interests. *Adv. Eng. Mater.* **2020**, *22*, 2070017. [CrossRef]
11. Jáquez-Muñoz, J.M.; Gaona-Tiburcio, C.; Mendez-Ramirez, C.T.; Carrera-Ramirez, M.G.; Baltazar-Zamora, M.A.; Santiago-Hurtado, G.; Lara-Banda, M.; Estupiñan-Lopez, F.; Nieves-Mendoza, D.; Almeraya-Calderon, F. Corrosion of Anodized Titanium Alloys. *Coatings* **2024**, *14*, 809. [CrossRef]
12. Han, X.; Ma, J.; Tian, A.; Wang, Y.; Li, Y.; Dong, B.; Tong, X.; Ma, X. Surface modification techniques of titanium and titanium alloys for biomedical orthopaedics applications: A review. *Colloids Surf. B Biointerfaces* **2023**, *227*, 113339. [CrossRef]
13. O'Keeffe, C.; Kotlarz, M.; Gonçalves, I.F.; Lally, C.; Kelly, D.J. Chemical etching of Ti-6Al-4V biomaterials fabricated by selective laser melting enhances mesenchymal stromal cell mineralization. *J. Biomed. Mater. Res. Part A.* **2024**, *112*, 1548–1564. [CrossRef] [PubMed]
14. Gao, Y.; Shen, K.; Wang, X. Microstructural evolution of low-pressure plasma-sprayed Ti–6Al–4V coatings after heat treatment. *Surf. Coat. Technol.* **2020**, *393*, 125792. [CrossRef]
15. Dockrat, U.; Ntsoane, T.P.; Malherbe, J.B.; Bam, L.C.; Thabethe, T.T. Investigating biomimetic coatings on Ti-6Al-4V substrates. *J. Alloy Compd. Commun.* **2025**, *7*, 100082. [CrossRef]
16. Cely-González, A.; Pineda, Y.; Gómez-Puentes, O. Anodization of Ti6Al4V alloy manufactured by 3D printing and evaluation of corrosion and wear properties. *DYNA* **2022**, *89*, 76–83. [CrossRef]
17. Diamanti, M.; Sebastiani, M.; Mangione, V.; Del Curto, B.; Pedeferri, M.; Bemporad, E.; Cigada, A.; Carassiti, F. Multi-step anodizing on Ti6Al4V components to improve tribomechanical performances. *Surf. Coat. Technol.* **2013**, *227*, 19–27. [CrossRef]

18. Lestari, F.; Rian, Y.; Pramono, A.; Rokhmanto, F.; Kartika, I.; Thaha, Y. Surface Modification of Ti-6Al-4V Alloy By Anodization Technique at Low Potential to Produce Oxide Layer. *J. Electron. Electromed. Eng. Med. Inform.* **2020**, *2*, 93–100. [CrossRef]
19. Dolimont, A.; Michotte, S.; Rivière-Lorphèvre, E.; Ducobu, F.; Vivès, S.; Godet, S.; Henkes, T.; Filippi, E. Influence on surface characteristics of electron beam melting process (EBM) by varying the process parameters. *AIP Conf. Proc.* **2017**, *1896*, 40010. [CrossRef]
20. Ran, J.; Jiang, F.; Sun, X.; Chen, Z.; Tian, C.; Zhao, H. Microstructure and Mechanical Properties of Ti-6Al-4V Fabricated by Electron Beam Melting. *Crystals* **2020**, *10*, 972. [CrossRef]
21. Hernández-Nava, E.; Smith, C.; Derguti, F.; Tammas-Williams, S.; Leonard, F.; Withers, P.; Todd, I.; Goodall, R. The effect of defects on the mechanical response of Ti-6Al-4V cubic lattice structures fabricated by electron beam melting. *Acta Mater.* **2016**, *108*, 279–292. [CrossRef]
22. Tamayo, J.A.; Riascos, M.; Vargas, C.A.; Baena, L.M. Additive manufacturing of Ti6Al4V alloy via electron beam melting for the development of implants for the biomedical industry. *Heliyon* **2021**, *7*, e06892. [CrossRef]
23. Ataee, A.; Li, Y.; Song, G.; Wen, C. Metal scaffolds processed by electron beam melting for biomedical applications. In *Metallic Foam Bone*; Elsevier: Amsterdam, The Netherlands, 2017; pp. 83–110.
24. DebRoy, T.; Wei, H.L.; Zuback, J.S.; Mukherjee, T.; Elmer, J.W.; Milewski, J.O.; Beese, A.M.; Wilson-Heid, A.; De, A.; Zhang, W. Additive manufacturing of metallic components—Process, structure and properties. *Progress in Materials Science* **2018**, *92*, 112–224. [CrossRef]
25. Behjat, A.; Sanaei, S.; Mosallanejad, M.H.; Atapour, M.; Sheikholeslam, M.; Saboori, A.; Iuliano, L. A novel titanium alloy for load-bearing biomedical implants: Evaluating the antibacterial and biocompatibility of Ti536 produced via electron beam powder bed fusion additive manufacturing process. *Biomater Adv.* **2024**, *163*, 213928. [CrossRef]
26. Carolo, L.C.B.; Cooper, O.R.E. A review on the influence of process variables on the surface roughness of Ti-6Al-4V by electron beam powder bed fusion. *Addit. Manuf.* **2022**, *59*, 103103.
27. Takase, A.; Ishimoto, T.; Morita, N.; Ikeo, N.; Nakano, T. Comparison of Phase Characteristics and Residual Stresses in Ti-6Al-4V Alloy Manufactured by Laser Powder Bed Fusion (L-PBF) and Electron Beam Powder Bed Fusion (EB-PBF) Techniques. *Crystals* **2021**, *11*, 796. [CrossRef]
28. Li, H.; Liang, X.; Li, Y.; Lin, F. Performance of High-Layer-Thickness Ti6Al4V Fabricated by Electron Beam Powder Bed Fusion under Different Accelerating Voltage Values. *Materials* **2022**, *15*, 1878. [CrossRef]
29. Schur, R.; Ghods, S.; Wisdom, C.; Pahuja, R.; Montelione, A.; Arola, D.; Ramulu, M. Mechanical anisotropy and its evolution with powder reuse in Electron Beam Melting AM of Ti6Al4V. *Mater. Des.* **2021**, *200*, 109450. [CrossRef]
30. Silvestri, A.T.; Foglia, S.; Borrelli, R.; Franchitti, S.; Pirozzi, C.; Astarita, A. Electron beam melting of Ti6Al4V: Role of the process parameters under the same energy density. *J. Manuf. Process* **2020**, *60*, 162–179. [CrossRef]
31. Antonysamy, A.A.; Meyer, J.; Prangnell, P.B. Effect of build geometry on the β-grain structure and texture in additive manufacture of Ti6Al4V by selective electron beam melting. *Mater. Charact.* **2013**, *84*, 153–168. [CrossRef]
32. Saboori, A.; Tognoli, E.; Galati, M.; Denti, L. Electron beam powder bed fusion of Ti–6Al–2Sn–4Zr–2Mo alloy: Microstructure evolution and high-temperature mechanical properties. *Prog. Addit. Manuf.* **2025**, *10*, 6627–6641. [CrossRef]
33. Cantaboni, F.; Battini, D.; Hauber, K.Z.; Ginestra, P.S.; Tocci, M.; Avanzini, A.; Ceretti, E.; Pola, A. Mechanical and microstructural characterization of Ti6Al4V lattice structures with and without solid shell manufactured via electron beam powder bed fusion. *Int. J. Adv. Manuf. Technol.* **2024**, *131*, 1289–1301. [CrossRef]
34. Manco, E.; Scherillo, F.; Franchitti, S.; Borrelli, R. Improving Surface Quality and Fatigue Life of Electron Beam Melted Ti6Al4V by Chemical Machining. *J. Mater. Eng. Perform.* **2024**, *33*, 2552–2561. [CrossRef]
35. Behjat, A.; Saboori, A.; Galati, M.; Iuliano, L. The electrochemical behaviour of Ti-48Al-2Cr-2Nb produced by electron beam powder bed fusion process. *Intermetallics* **2024**, *175*, 108472. [CrossRef]
36. Mosallanejad, M.H.; Ghanavati, R.; Behjat, A.; Taghian, M.; Saboori, A.; Iuliano, L. Untapped Opportunities in Additive Manufacturing with Metals: From New and Graded Materials to Post-Processing. *Metals* **2024**, *14*, 425. [CrossRef]
37. Chern, A.H.; Nandwana, P.; McDaniels, R.; Dehoff, R.R.; Liaw, P.K.; Tryon, R.; Duty, C.E. Build orientation, surface roughness, and scan path influence on the microstructure, mechanical properties, and flexural fatigue behavior of Ti–6Al–4V fabricated by electron beam melting. *Mater. Sci. Eng. A* **2020**, *772*, 138740. [CrossRef]
38. Sepe, R.; Franchitti, S.; Borrelli, R.; Di Caprio, F.; Armentani, E.; Caputo, F. Correlation between real geometry and tensile mechanical behaviour for Ti6Al4V electron beam melted thin specimens. *Theor. Appl. Fract. Mech.* **2020**, *107*, 102519. [CrossRef]
39. Valencia-Cadena, A.; García-Blanco, M.; Reschenhofer, B.; Barreneche, C.; Skerbis, P.; Leitl, P.; Santamaría, P.; Roa, J. In-depth study of the dry-anodizing process on Ti6Al4V alloys: Effect of the acid content and electrical parameters. *Surf. Coat. Technol.* **2025**, *499*, 131767. [CrossRef]

40. Vásquez, F.A.; Ocampo, R.A.; Bedoya, N.; Gil, A.A.Z.; Botero, C.; Gómez, M.; Castaño, J.G.; Tamayo, J.A. Electrochemical characterization of $TiO_2$ nanotubes formed on Ti6Al4V manufactured by PBF-EB or forging. *Prog. Addit. Manuf.* **2025**, *10*, 3629–3639. [CrossRef]
41. Moradi, A.; Tajalli, S.; Mosallanejad, M.; Saboori, A. Intelligent laser-based metal additive manufacturing: A review on machine learning for process optimization and property prediction. *Int. J. Adv. Manuf. Technol.* **2024**, *136*, 527–560. [CrossRef]
42. Chastand, V.; Quaegebeur, P.; Maia, W.; Charkaluk, E. Comparative study of fatigue properties of Ti-6Al-4V specimens built by electron beam melting (EBM) and selective laser melting (SLM). *Mater. Charact.* **2018**, *143*, 76–81. [CrossRef]
43. Liu, S.; Shin, Y.C. Additive manufacturing of Ti6Al4V alloy: A review. *Mater. Des.* **2019**, *164*, 107552. [CrossRef]
44. Łępicka, M.; Grądzka-Dahlke, M.; Sobolewski, A. The effect of anodizing conditions on the corrosion resistance of Ti6Al4V titanium alloy. *Mater. Test.* **2015**, *57*, 393–397. [CrossRef]
45. Gomez-Vega, J.; Saiz, E.; Tomsia, A.; Marshall, G. Bioactive glass coatings with hydroxyapatite and Bioglass® particles on Ti-based implants. 1. Processing. *Biomaterials* **2000**, *21*, 105–111. [CrossRef] [PubMed]
46. Yuan, P.; Chen, M.; Lu, X.; Yang, H.; Wang, L.; Bai, T.; Zhou, W.; Liu, T.; Yu, S. Application of advanced surface modification techniques in titanium-based implants: Latest strategies for enhanced antibacterial properties and osseointegration. *J. Mater. Chem. B* **2024**, *12*, 10516–10549. [CrossRef]
47. Avila, J.D.; Stenberg, K.; Bose, S.; Bandyopadhyay, A. Hydroxyapatite reinforced Ti6Al4V composites for load-bearing implants. *Acta Biomater.* **2021**, *123*, 379–392. [CrossRef]
48. Osafo, S.A.; Asumadu, T.; Klenam, D.; Etinosa, P.; Obayemi, J.D.; Agyei-Tuffour, B.; Yaya, A.; Dodoo-Arhin, D.; Eluu, S.C.; Soboyejo, W. Tribological properties of hydroxyapatite-coated nanorods on Ti-6Al-4V surfaces. *Sci. Rep.* **2025**, *15*, 19113. [CrossRef]
49. Khrapov, D.; Kozadayeva, M.; Manabaev, K.; Panin, A.; Sjöström, W.; Koptyug, A.; Mishurova, T.; Evsevleev, S.; Meinel, D.; Bruno, G.; et al. Different Approaches for Manufacturing Ti-6Al-4V Alloy with Triply Periodic Minimal Surface Sheet-Based Structures by Electron Beam Melting. *Materials* **2021**, *14*, 4912. [CrossRef]
50. Ikreedeegh, R.R.; Hossen, M.A.; Tahir, M.; Aziz, A.A. A comprehensive review on anodic $TiO_2$ nanotube arrays (TNTAs) and their composite photocatalysts for environmental and energy applications: Fundamentals, recent advances and applications. *Coord. Chem. Rev.* **2024**, *499*, 215495. [CrossRef]
51. Kokubo, T.; Takadama, H. Simulated Body Fluid (SBF) as a Standard Tool to Test the Bioactivity of Implants. In *Handbook of Biomineralization: Medical and Clinical Aspects*; Wiley: Hoboken, NJ, USA, 2008; pp. 97–109.
52. Donachie, M. *Titanium: A Technical Guide*, 2nd ed.; ASM International: Almere, The Netherlands, 2000.
53. Torres-Avila, I.P.; Padilla-Martínez, I.I.; Pérez-Hernández, N.; Bañuelos-Hernández, A.E.; Velázquez, J.C.; Castrejón-Flores, J.L.; Hernández-Sánchez, E. Surface Modification of the Ti-6Al-4V Alloy by Anodic Oxidation and Its Effect on Osteoarticular Cell Proliferation. *Coatings* **2020**, *10*, 491. [CrossRef]
54. Mehrotra, S.; Kalyan, D.; Makineni, S.K.; Santra, S. Oxide growth characteristics, kinetics and mechanism of rutile formation on pure titanium. *Vacuum* **2024**, *219*, 112682. [CrossRef]
55. Jia, J.; Yamamoto, H.; Okajima, T.; Shigesato, Y. On the Crystal Structural Control of Sputtered $TiO_2$ Thin Films. *Nanoscale Res. Lett.* **2016**, *11*, 324. [CrossRef]
56. Padayachee, D.; Mahomed, A.; Singh, S.; Friedrich, H. The effect of the $TiO_2$ anatase:rutile ratio and interface for the oxidative activation of n-octane. *ACS Catal.* **2020**, *10*, 2211–2220. [CrossRef]
57. Ghani, T.; Mehmood, M.; Kanwal, H.; Naz, M.Y.; Bashir, S. Photovoltaic Performance of $TiO_2$ Nanotubes Anodized under Different Voltages. *Materials Proceedings* **2024**, *17*, 24. [CrossRef]
58. Cao, W.; Chen, K.; Xue, D. Highly Ordered $TiO_2$ Nanotube Arrays with Engineered Electrochemical Energy Storage Performances. *Materials* **2021**, *14*, 510. [CrossRef]
59. Sarraf, M.; Razak, B.A.; Ghasemi, M.; Nezhad, E.Z.; Hashemi, R.; Bae, S. Systematic microstructure modification effect on nanomechanical, tribology, corrosion, and biomineralization behavior by optimized anodic alumina nanotubes coated Ti–6Al–4V alloy. *Ceram. Int.* **2023**, *49*, 23437–23455. [CrossRef]
60. Dikova, T.; Nikolova, M.; Yankov, E. Adhesion Analysis of Titanium Oxide Nanocoatings on Titanium Surface. *Mater. Sci. Non-Equilib. Phase Transform.* **2016**, *2*, 46–51.
61. Pereira, B.L.; Beilner, G.; Lepienski, C.M.; de Souza, G.B.; Kuromoto, N.K.; Szameitat, E.S.; Peng, A.N.S.; Lee, J.Y.; Claro, A.P.R.A.; Nugent, M.J. Scratch-resistant and well-adhered nanotube arrays produced via anodizing process on β-titanium alloy. *Mater. Today Commun.* **2021**, *26*, 101947. [CrossRef]
62. Cui, X.; Kim, H.-M.; Kawashita, M.; Wang, L.; Xiong, T.; Kokubo, T.; Nakamura, T. Apatite formation on anodized Ti6Al4V alloy in simulated body fluid. *Met. Mater. Int.* **2010**, *16*, 407–412. [CrossRef]

63. Sarraf, M.; Sukiman, N.L.; Bushroa, A.R.; Nasiri-Tabrizi, B.; Dabbagh, A.; Abu Kasim, N.H.; Basirun, W.J. In vitro bioactivity and corrosion resistance enhancement of Ti-6Al-4V by highly ordered $TiO_2$ nanotube arrays. *J. Aust. Ceram. Soc.* **2019**, *55*, 187–200. [CrossRef]
64. Nogueira, R.P.; Uchoa, J.D.; Hilario, F.; Santana-Melo, G.d.F.; de Vasconcellos, L.M.R.; Marciano, F.R.; Roche, V.; Junior, A.M.J.; Lobo, A.O. Characterization of Optimized $TiO_2$ Nanotubes Morphology for Medical Implants: Biological Activity and Corrosion Resistance. *Int. J. Nanomed.* **2021**, *16*, 667–682. [CrossRef] [PubMed]